Wind-Wave Effects on Estuarine Turbulence: A Comparison of Observations and Second-Moment Closure Predictions

ALEXANDER W. FISHER

Horn Point Laboratory, University of Maryland Center for Environmental Science, Cambridge, Maryland, and Department of Geography, University of California, Santa Barbara, Santa Barbara, California

LAWRENCE P. SANFORD

Horn Point Laboratory, University of Maryland Center for Environmental Science, Cambridge, Maryland

MALCOLM E. SCULLY

Applied Ocean Physics and Engineering, Woods Hole Oceanographic Institution, Woods Hole, Massachusetts

(Manuscript received 20 July 2017, in final form 24 January 2018)

ABSTRACT

Observations of turbulent kinetic energy, dissipation, and turbulent stress were collected in the middle reaches of Chesapeake Bay and were used to assess second-moment closure predictions of turbulence generated beneath breaking waves. Dissipation scaling indicates that the turbulent flow structure observed during a 10-day wind event was dominated by a three-layer response that consisted of 1) a wave transport layer, 2) a surface log layer, and 3) a tidal, bottom boundary layer limited by stable stratification. Below the wave transport layer, turbulent mixing was limited by stable stratification. Within the wave transport layer, where dissipation was balanced by a divergence in the vertical turbulent kinetic energy flux, the eddy viscosity was significantly underestimated by second-moment turbulence closure models, suggesting that breaking waves homogenized the mixed surface layer to a greater extent than the simple model of TKE diffusing away from a source at the surface. While the turbulent transport of TKE occurred largely downgradient, the intermittent downward sweeps of momentum generated by breaking waves occurred largely independent of the mean shear. The underprediction of stress in the wave transport layer by second-moment closures was likely due to the inability of the eddy viscosity model to capture the nonlocal turbulent transport of the momentum flux beneath breaking waves. Finally, the authors hypothesize that large-scale coherent turbulent eddies played a significant role in transporting momentum generated near the surface to depth.

1. Introduction

Wind-driven flows can dominate subtidal material exchange in estuarine environments including oxygen (Scully 2010a,b, 2013), sediments (Chen et al. 2009), and salt (Geyer 1997; Scully et al. 2005; Chen and Sanford 2009; Li and Li 2011, 2012). Breaking surface waves serve as the principal pathway through which momentum and mechanical energy are transferred from the atmosphere to the oceanic surface boundary layer (Melville 1996) and, as such, can play a pivotal role in structuring turbulent mixing beneath the water surface. Within the surface boundary layer, surface waves can influence hydrodynamics in three principal ways (Jones and Monismith 2008a): 1) direct injection of turbulent kinetic energy (TKE) beneath breaking waves (e.g., Terray et al. 1996), 2) enhanced vertical transport driven by coherent turbulent eddies such as Langmuir turbulence (Craik and Leibovich 1976; Leibovich 1983), and 3) Reynolds stresses generated by nonlinearities in the surface wave field (Magnaudet and Thais 1995). This study examines the effects of 1 on turbulence profiles measured in Chesapeake Bay and discusses the interplay of 1 and 2 in governing momentum and energy transfer in the wave-affected surface layer.

Corresponding author: Alexander W. Fisher, awfisher@ucsb.edu

Publisher's Note: This article was revised on 20 April 2018 to correct a production error that caused misidentification of a reference, whose citation was then abbreviated incorrectly throughout the article when originally published.

DOI: 10.1175/JPO-D-17-0133.1

Injection of TKE to the oceanic surface boundary layer by breaking waves can result in turbulent kinetic energy dissipation rates that are orders of magnitude larger (Kitaigorodskii et al. 1983; Agrawal et al. 1992; Anis and Moum 1995; Terray et al. 1996; Drennan et al. 1996; Feddersen et al. 2007; Jones and Monismith 2008a; Gerbi et al. 2009; Gemmrich 2010) than those produced by shear production near a rigid boundary (Hinze 1975). Observational constraints have made directly measuring turbulent fluxes difficult, and as a result most studies have been constrained to an analysis of dissipation and turbulent vertical velocity statistics. Several studies conducted in the coastal ocean have shown that the region of elevated dissipation beneath breaking waves can occupy a significant fraction of the water column (Jones and Monismith 2008a; Young et al. 2005; Scully et al. 2016).

During an experiment conducted in the middle reaches of Chesapeake Bay in the fall of 2013, breaking waves dominated the transfer of momentum and energy in the oceanic surface layer (Scully et al. 2016), and coherent turbulent structures consistent with Langmuir turbulence were documented (Scully et al. 2015). Building on analyses presented in a series of manuscripts describing wind-forced responses observed during this experiment (Scully et al. 2015, 2016; Fisher et al. 2017), this paper examines the effects of wind waves on vertical profiles of estuarine turbulence and compares observations to the predictions of second-moment turbulence closure schemes.

The paper is organized as follows: 1) background material on the scaling relations used describing turbulence beneath breaking waves and second-moment turbulence closure schemes used in circulation modeling; 2) field data collection and analysis methods; 3) results of the experiment, which relate the observed TKE budget to parameters used in second-moment closures (and an overview of the turbulent structure of the wind-driven response observed at the tower site); 4) a discussion of the turbulent transport of nonlocal TKE and momentum and its impact on turbulence modeling; and 5) a summary of research findings and conclusions.

2. Background

a. The wave transport layer

The turbulent kinetic energy equation for a wave-affected surface layer can be expressed as follows (McWilliams et al. 1997):

$$\frac{Dk}{Dt} = -\langle u_i' w' \rangle \frac{\partial U_i}{\partial z} - \langle u_i' w' \rangle \frac{\partial U_{\mathrm{Si}}}{\partial z} - \frac{g}{\rho_0}\langle \rho' w' \rangle - \frac{\partial}{\partial z}\left(\frac{1}{2}\langle u_j'^2 w \rangle + \frac{1}{\rho_0}\langle p' w' \rangle\right) - \varepsilon, \tag{1}$$

(i) (ii) (iii) (iv) (v) (vi)

where mean and fluctuating components of velocity, density, and pressure have been partitioned using Reynolds decomposition, such that $u = \langle u \rangle + u'$, where angle brackets denote a time average such that $\langle u \rangle = U$ and $\langle u' \rangle = 0$. The variables g and ρ_0 represent gravity and the reference density of seawater ($1025\,\mathrm{kg\,m^{-3}}$), respectively. Turbulent kinetic energy is defined as $k = (1/2)(\langle u'^2 \rangle + \langle v'^2 \rangle + \langle w'^2 \rangle)$. The terms on the right-hand side of Eq. (1) are (i) Eulerian shear production, (ii) Stokes shear production, (iii) buoyancy flux, the divergence of the (iv) turbulent TKE transport by velocity fluctuations and (v) turbulent TKE transport by pressure fluctuations or pressure work, and (vi) dissipation. We refer to the sum of terms (iv) and (v) as the total turbulent TKE flux. Note that we have omitted the viscous TKE transport term from Eq. (1).

By assuming that wave breaking is the principal source of TKE and that breaking injects energy to a depth on the order of the significant wave height, Terray et al. (1996) postulated that the wave-affected surface layer (WASL) consists of two sublayers: 1) a wave-breaking sublayer in which direct injection of TKE near the surface leads to region of constant dissipation and negligible shear production and 2) a wave transport layer where TKE is transported away from the surface by turbulent eddies such that dissipation is balanced by the vertical divergence of TKE transport (Terray et al. 1996).

Collapsing their data using the estimated wind energy input to surface waves F_0, the significant wave height H_S, and the depth below the surface z, Terray et al. (1996) postulated a dissipation scaling for the wave transport layer:

$$\frac{\varepsilon H_S}{F_0} = c\left(\frac{|z|}{H_S}\right)^{-b}, \tag{2}$$

where c and b were determined to be 0.3 and 2, respectively. We note that for the remainder of this paper, we will use an upward-positive z coordinate system with $z = 0$ at the mean (burst averaged) free surface. Observations have shown consistency with Eq. (2) for deep-water wave-breaking conditions in both young, fetch-limited wind seas (Terray et al. 1996; Jones and Monismith 2008b) and more developed wind seas (Drennan et al. 1996).

The scaling in Eq. (2) is valid over a range of depths determined by two factors: 1) the depth-integrated dissipation within the wave-affected surface layer matches the downward flux of TKE at the surface due to wave energy dissipation, and 2) as shear production becomes more dominant, the dissipation rate reduces to wall layer scaling:

$$\varepsilon = \frac{u_{*_S}^3}{k|z|}, \tag{3}$$

where u_{*_S} is the surface shear velocity, given by $u_{*_S} = \sqrt{\tau_{z=0}/\rho}$, and $k = 0.41$ is the von Kármán constant. Below the wave transport layer, the TKE budget is expected to reduce to a balance between shear production and dissipation consistent with a surface log layer. Field measurements (Agrawal et al. 1992) and laboratory studies (Monismith and Magnaudet 1998) have shown that dissipation scales with wall layer theory below the wave transport layer, but in shallow coastal environments the wave transport layer may also transition directly to a bottom boundary layer (Jones and Monismith 2008b). The Terray et al. (1996) scaling assumes that one-half of the surface TKE flux generated by wave breaking reaches the wave transport layer. Using the integral constraint on the wave transport layer, Terray et al. (1996) postulated that the depth of the wave-breaking sublayer (constant dissipation layer) was $z_0 = -0.6H_S$ for the fetch-limited wind seas observed during the experiment—a result consistent with the laboratory results of Rapp and Melville (1990). We note that z_0 is a displacement height, not a roughness parameter, and represents the base of the active breaking and bubble entrainment sublayer.

The assumption of a constant dissipation layer very near the surface has been challenged by the wave-following measurements of Gemmrich and Farmer (1999), Soloviev and Lukas (2003), and Gemmrich and Farmer (2004), which suggest that the value of z_0 should be much less than the ratio of $|z_0/H_S| = 0.6$ imposed by Terray et al. (1996) scaling. Furthermore, modifications to the scaling in Eq. (2) are needed when the model is applied to mixed seas with significant swell energy (Greenan et al. 2001).

b. Turbulence closure models

In ocean circulation models, second-moment closure schemes are often used to parameterize turbulence (Warner et al. 2005). Most closure models parameterize the total turbulent TKE flux as a downgradient process reducing Eq. (1) to

$$\frac{Dk}{Dt} = P + B + F_{\mathrm{TKE}} - \varepsilon, \tag{4}$$

where P is shear production, B is buoyancy production, and F_{TKE} represents the vertical divergence of the sum of turbulent and viscous TKE transport. Second-moment closure schemes solve Eq. (4) in combination with a similar transport equation for dissipation (k–ε; Rodi 1987), turbulent length scale (k–kl; Mellor and Yamada 1982), or turbulent velocity (k–ω; Wilcox 1988). Some attempts have been made to incorporate the effects of Langmuir turbulence into second-moment closure schemes (via the Stokes production term) using Mellor–Yamada-style closure schemes (Kantha and Clayson 2004; Harcourt 2015).

Several studies have used one-dimensional (1D) vertical models with second-moment closure schemes to simulate the effects of wave breaking with good accuracy (Craig and Banner 1994; Craig 1996; Burchard 2001; Umlauf and Burchard 2003; Stips et al. 2005). However, most of these studies focused on reproducing measured dissipation profiles and did not directly compare observed and modeled momentum fluxes due to limited data. The landmark model of Craig and Banner (1994) reproduced dissipation profiles observed by Agrawal et al. (1992), Anis and Moum (1992), and Osborn et al. (1992) reasonably well using a Mellor–Yamada closure scheme. However, these datasets did not include the elevated near-surface dissipation rates measured by Terray et al. (1996) or Drennan et al. (1996). Terray et al. (1999) adapted the original Craig and Banner (1994) model to match these observations through a modification to the expression for turbulent length scale (Terray et al. 1999; Jones and Monismith 2008b).

Within second-moment closure schemes, the vertical transport of momentum and buoyancy is modeled as a downgradient process (Rodi 1980):

$$-\langle u'w'\rangle = A_z \frac{\partial U}{\partial z}, \quad \text{and} \tag{5}$$

$$-\frac{g}{\rho_0}\langle \rho'w'\rangle = K_z N^2, \tag{6}$$

where N is the Brunt–Väisälä frequency. Similarly, the transport term F_{TKE} is typically modeled as a downgradient process such that (Umlauf and Burchard 2003)

$$F_{\mathrm{TKE}} = \frac{\partial}{\partial z}\left(\frac{Az}{\sigma_k}\frac{\partial k}{\partial z}\right), \tag{7}$$

where σ_k is a turbulent Schmidt number expressing the ratio of momentum diffusivity to TKE diffusivity. The eddy viscosity A_z and the eddy diffusivity K_z are proportional to the product of a turbulent velocity scale and a turbulent length scale, such that

$$A_z = c_\mu \frac{k^2}{\varepsilon}, \quad \text{and} \tag{8}$$

$$K_z = c'_\mu \frac{k^2}{\varepsilon}, \tag{9}$$

where c_μ is a nondimensional parameter known as the stability function and the turbulent velocity scales as $k^{1/2}$. The macrolength scale for energy-containing eddies then becomes

$$l = c_L \frac{k^{3/2}}{\varepsilon}, \tag{10}$$

where $c_L = (c^0_\mu)^{3/4}$ and $c^0_\mu = 0.09$ is the value of the stability function resulting from a $P = \varepsilon$ balance in the TKE equation (Burchard and Bolding 2001, hereinafter BB01). Assuming that the momentum flux is transported by the same family of eddies that govern TKE dynamics, the master length scale modeled in Eq. (10) is equivalent to the Prandtl mixing length near rigid boundaries (Mellor and Yamada 1982).

Umlauf and Burchard (2003) demonstrate that the formulation of different second-moment closure schemes is structurally similar regardless of the dynamical equation used in conjunction with the TKE equation. Therefore the formulation of the stability function, rather than the choice of model, influences model performance (Burchard et al. 1998). Some modeling studies of wave transport layers have used a constant stability function (Craig and Banner 1994), but other approaches assume that the stability functions are functions of nondimensional shear α_S and stratification α_N (Burchard 2001):

$$\alpha_S = S^2 \frac{k^2}{\varepsilon^2}, \quad \text{and} \tag{11}$$

$$\alpha_N = N^2 \frac{k^2}{\varepsilon^2}. \tag{12}$$

Using the definition of eddy viscosity and Eqs. (5), (8), and (11), the relationship between the momentum flux and TKE stress can be shown as follows (Scully et al. 2011):

$$\frac{-\langle u'w' \rangle}{k} = \sqrt{c_\mu \frac{P}{\varepsilon}} = c_\mu \sqrt{\alpha_S}, \tag{13}$$

where the ratio of the Reynolds stress to TKE is known as the nondimensional stress and expresses the efficiency of turbulent motions in producing a momentum flux (Scully et al. 2011). Stability functions are therefore used to relate TKE dynamics to the momentum flux within second-moment closure models.

The assumption that turbulence is in local equilibrium leads to "quasi equilibrium" stability functions that retain the full TKE equation but whose solutions are limited to turbulence in which $P + B = \varepsilon$. In terms of stability functions, this local equilibrium state can be expressed as $c_\mu \alpha_S - c'_\mu \alpha_N = 1$ (BB01). Most numerical circulation models employ quasi-equilibrium stability functions (Chen et al. 2003; Warner et al. 2005), but nonequilibrium formulations (discussed below) are becoming increasingly common in coastal simulations (Warner et al. 2005).

Nonequilibrium stability functions, such as that proposed by Canuto et al. (2001, hereafter CA01), better account for departures from a $P + B = \varepsilon$ balance (Umlauf and Burchard 2003; Scully et al. 2011) and are more suitable for strongly stratified estuarine flows (Scully et al. 2011) and wave transport layers where vertical divergence in the total turbulent TKE flux is a dominant term in the TKE budget and turbulent TKE transport may be countergradient (Scully et al. 2016). Burchard (2001) used the CA01 stability function formulation to reproduce dissipation profiles beneath breaking waves with good accuracy. A detailed discussion of nonequilibrium formulations of the stability function can be found in BB01.

3. Methods

a. Field observations

At the center of an extensive field experiment conducted in the fall of 2013, a turbulence tower was deployed on the western shoal of Chesapeake Bay (38°27′39″N, 76°24′44″W) in a 14-m-deep region of slowly varying bathymetry. The tower was held vertically rigid using four guy wires, which were secured to the top of the tower and anchored to 450-kg railcar wheels (Scully et al. 2015; Fisher et al. 2017). The tower was deployed on 18 September 2013 and recovered on 29 October 2013. A schematic of the tower and map of the deployment site are shown in Scully et al. (2015) and Fisher et al. (2017).

A vertical array of Nortek vector acoustic Doppler velocimeters (ADVs) provided direct measurements of turbulent fluxes and mean velocities (burst averages). The downward-looking ADV heads were mounted on 1-m aluminum arms attached to the tower, spaced ~2 m apart, starting at approximately 1.7 m below the mean water surface. The aluminum arms were oriented due west, and the pressure housings of the ADVs were mounted away from the sensor head on the arms to minimize flow disturbance near sampling volumes. The pressure sensor, located in the end cap of the housing, was 25 cm from the sampling volume of the ADV heads. The ADVs recorded three-dimensional velocity and pressure data at 32 Hz in 28-min bursts centered 30 min apart. Time series of burst-averaged pressure data from the ADV array were used to reference the depth of the tower array to the time-variable free surface. High-frequency variability due to surface gravity waves, however, was not accounted for in this calculation. Temperature and conductivity measurements were

collected every 5 min using six Seabird MicroCat CTDs mounted to the tower with sampling volumes aligned to the ADV sensor heights.

Direct measurements of the total wind stress and sensible heat flux were collected by a Campbell Scientific CSAT3 ultrasonic anemometer with fine-wire thermocouple deployed on an aerial platform atop the tower. The anemometer was oriented due north and had a sampling volume elevation of ~2.82 m MSL. The system sampled the 3D velocity field and air temperature at 10 Hz continuously. Atmospheric measurements of wind stress were calculated by integrating velocity cospectra for frequencies less than 2 Hz in 30-min blocks (Rieder et al. 1994). The sensitivity of vertical flux measurements to variations in vertical velocity prompted a tilt correction using the planar fit method (Wilczak et al. 2001) on daily subranges of the anemometer data as described in Fisher et al. (2015). The anemometer was deployed on 25 September 2013 and recovered on 28 October 2013.

Directional wave spectra were calculated from velocity and pressure records from the uppermost ADV ($z = -1.7$ m) using linear wave theory and the Directional Wave Spectra (DIWASP) toolkit (Johnson 2002). For details on wave processing used in this analysis, see Fisher et al. (2017). Vertical profiles of Stokes drift velocity were calculated from directional wave spectra following Kenyon (1969).

The surface TKE flux F_0 was estimated as the wind input into the surface wave field:

$$F_0 = g \int_0^{2\pi} \int_0^{\omega_{\max}} \beta F(\omega, \theta)\, \partial\omega\, \partial\theta, \tag{14}$$

where β is the e-folding scale for the growth rate of wave energy formulated by Plant (1982) and $F(\omega, \theta)$ is the observed directional wave spectra. The surface TKE flux can also be expressed using an empirical wave energy factor G_T (Craig and Banner 1994), which is often assumed to be wave-age dependent (Drennan et al. 1996; Terray et al. 1996). Following Kundu (1980), the wave energy factor was calculated using a least squares regression of estimated F_0 values and the directly measured wind stress, where u_{*_w} is the water-side shear velocity of the total wind stress, such that

$$F_0 = G_T u_{*_w}^3. \tag{15}$$

As discussed in Fisher et al. (2017), significant momentum storage within the surface wave field can occur in the middle reaches of Chesapeake Bay as a result of a horizontal divergence of wave energy transport that develops as a result of anisotropic fetch limitation. Accounting for momentum storage in the surface wave field was needed to close the air–sea momentum budget at the tower site and should therefore be considered when using F_0 as a scaling for dissipation within the wave transport layer. The total wind energy input F_0 was adjusted for the departures from wind-wave equilibrium by using a ratio of the shear stress at the mean free surface to the total wind stress ($u_{*_s}^3/u_{*_w}^3$) calculated using interaction stress theory (Fisher et al. 2017), which reduced the surface TKE flux by an average of 8%. A linear regression of $u_{*_s}^3$ and the adjusted F_0 value yielded a mean wave energy factor (G_T) of 77.

b. Terms in the TKE budget

Terms within the TKE budget can be directly estimated using observed cospectra and mean shear measured by the vertical array of ADVs. Direct estimates of the buoyancy flux could not be made using measurements collected during this experiment. However, using the surface heat flux, Scully et al. (2015) indirectly estimated the buoyancy term and showed that it was two orders of magnitude smaller than observed dissipation rates (e.g., Scully et al. 2016). To avoid artificial enhancement of stress estimates from correlated wave orbital velocities, the integration of ADV burst velocity cospectra was limited to frequencies below the wave band, less than 0.1 Hz. Dissipation was estimated by fitting the semiempirical model of Kaimal et al. (1972) to vertical velocity spectra following the method outlined in Gerbi et al. (2009). The method fits the Kaimal et al. (1972) spectral model using inertial range scaling (Tennekes and Lumley 1972) and accounts for unsteady advection by orbital velocities using the analytical model of Lumley and Terray (1983). The Gerbi et al. (2009) approach extends the method outlined in Feddersen et al. (2007) to directional wave spectra and reverts to standard inertial range scaling in the absence of wave orbital velocities.

The pressure work term in Eq. (1) was measured using velocity and pressure records from the ADV array. A clear noise floor of ~10 Pa, estimated from observed pressure spectra at $f > 10$ Hz, was consistent between bursts and between instruments and was typically an order of magnitude lower than low-frequency ($f < 0.1$ Hz) pressure fluctuations during periods of strong wind and wave forcing (Scully et al. 2016). Dynamic pressure fluctuations recorded by the ADVs contain both real fluctuations caused by advective and local fluid accelerations and errors associated with flow around the pressure housing of the ADV, requiring a careful evaluation of contributions by environmental flow features and errors due to the limitations of data collection. Scully et al. (2016) determined that observed low-frequency pressure fluctuations measured at ~1.7 m below the surface were at least 3 times larger than the stagnation pressure, a plausible upper bound on the pressure error due to flow distortion around the canister

(Elliott 1972). Furthermore, low-frequency fluctuations measured near the surface and near the bed were strongly correlated while the stagnation pressures were not, indicating that the observed pressure fluctuations were consistent with real pressure fluctuations (Scully et al. 2016). We refer the reader to the appendix of Scully et al. (2016) for more details regarding the validation of pressure work measurements used in this study.

c. Data analysis conditions

The analysis period was constrained to three weeks spanning 25 September 2013 to 18 October 2013 due to the exhaustion of ADV batteries. Owing to the depth of the pressure sensor, reliable wave data provided by the uppermost ADV were limited to conditions when the significant wave height was greater than 15 cm and the peak period was greater than 1.6 s. Data analysis was limited to periods in which the atmospheric surface boundary layer was hydraulically rough ($\sqrt{\tau_w/\rho_{\text{air}}} > 0.103$) and when the observed wind speed was greater than 3 m s^{-1}. The ADV sensor heads were mounted on aluminum arms that were oriented due west (270°) and were nearly orthogonal to the principal flow axis at the tower site, which was 150°–330°. However, flows from the east-southeast could produce wakes from the tower that were sampled by the ADV array. To avoid possible contamination of the turbulence measurements, periods when the mean flow was directed west-northwest 250°–310° were omitted from the analysis (5% of observations).

Periods when the two-parameter least squares fit to vertical velocity spectra provided unrealistic physical values for the roll-off wavenumber and variance were omitted. Finally, as discussed in Gerbi et al. (2009), periods when the mean current was not strong enough to stop surface wave orbital velocities from advecting ADV sensor wakes back into the sampling volumes were omitted. Following Gerbi et al. (2009), the advective threshold used here was $U_d/\sigma_d > 3$, where σ is the wave orbital velocity variance in the downstream direction d. Approximately 44% of the deployment record (589 data points) satisfied all of these criteria and was used in the analysis.

4. Results

a. Deployment conditions

A 10-day nor'easter occurred between 6 and 16 October 2013 and dominated the wind and wave conditions recorded during the deployment. The event was characterized by winds blowing from the northeast to the north at an average wind speed of 7 m s^{-1}. Wind stress peaked at 0.31 Pa and averaged 0.13 Pa. The event generated a surface wave field that had a significant wave height of ~1 m and a typical peak wave period of 4 s. Tidal velocities were on the order of 0.5 m s^{-1} and were aligned with the central channel at 150°T. During periods of energetic wind mixing, density stratification was generally weak (top to bottom density difference of ~0.5 kg m^{-3}), except for persistent near-bottom stratification at $z \sim -10$ m. During the latter half of the nor'easter, the water column was moderately stratified (top to bottom density difference of ~3 kg m^{-3}). Values of N^2 were calculated from the vertical array of MicroCat CTDs, such that the shallowest estimate of N^2 was approximately 2.6 m below the surface. A summary of tower conditions observed during the deployment is presented in Fig. 1.

Wind and wave forcing generated a flow response within the estuary that resulted in near-surface shear that was much lower than expected for a logarithmic surface boundary layer (Fig. 2). A time series of the Eulerian shear measured between the top two ADVs ($z \sim -2.6$ m) shows that during periods of active wind and wave forcing, the Eulerian shear was significantly lower than surface log layer scaling: $\partial U/\partial z = u_{*_s}/k|z|$. We note that the second ADV was deployed at ~3.5 m and was in the wave transport layer approximately 50% of the analysis period; as such the results shown in Fig. 2 may overpredict the shear measured within the wave transport layer. Between 9 and 11 October, the near-surface Eulerian shear was nearly an order of magnitude lower than surface log layer scaling. This dramatic reduction in shear is consistent with the conceptual model of a shear-free transport layer and provides a basis for further analysis of scaling arguments used in describing a turbulent transport layer beneath breaking waves.

Scully et al. (2016) observed downward sweeps of along-wave momentum that coincided with elevated backscatter at the uppermost ADV during the experiment, which is consistent with bubble clouds being swept down by the injection of momentum beneath a breaking wave. Without direct video observations of whitecaps, we rely on a spectral estimate of breaking probability to determine the scales at which wave crests broke at the tower site during the experiment.

Breaking probability is defined as the ratio of the passage rate of breaking crests to total number of wave crests past a fixed point in space (Phillips 1985; Banner et al. 2002). For a range of wave scales, Banner et al. (2002) related the breaking probability to the azimuthal-integrated spectral saturation of the wave energy spectra $F(f)$:

$$B(f) = \frac{(2\pi)^4 f^5 F(f)}{2g^2}, \tag{16}$$

where $B(f)$ is a frequency-dependent saturation spectrum and f is frequency. The saturation spectrum is

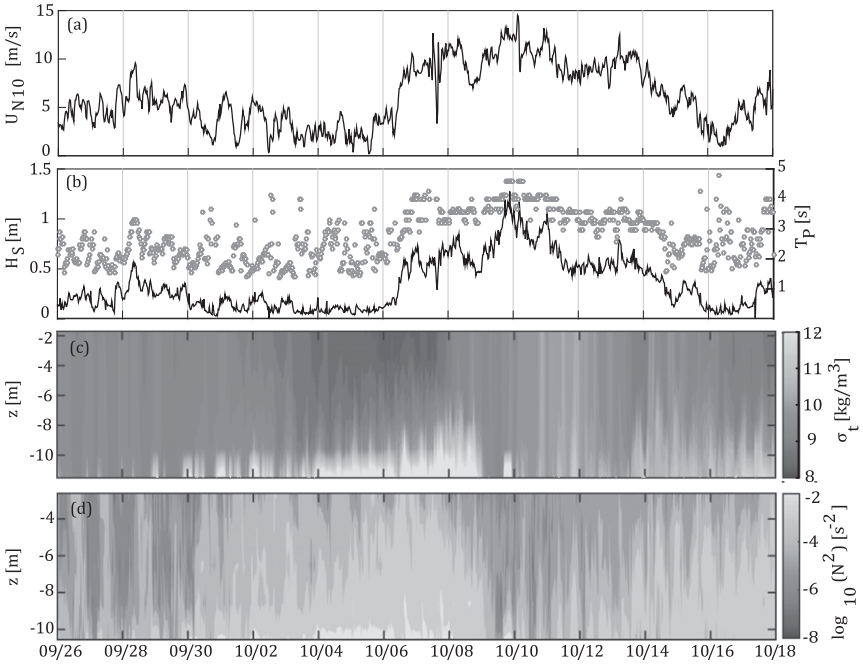

FIG. 1. Time series of deployment conditions: (a) 10-m neutral wind speed, (b) significant wave height and peak period, (c) density anomaly, and (d) N^2.

directly related to the wave mean square slope (mss) and therefore to overall wave steepness (Schwendeman et al. 2014). Comparing video observations of breaker occurrence to $B(f)$, Banner et al. (2002) determined that breaking occurred above a threshold value of $B(f)$ and that the breaking probability increased approximately linearly with $B(f)$. Normalizing $B(f)$ by the local angular spreading width of the wave spectrum $\theta(f)$ such that

$$\tilde{B} = \frac{B(f)}{\theta(f)} \tag{17}$$

resulted in a common critical breaking threshold of across wave scales of $B_{\mathrm{cr}} = 4.5 \times 10^{-3}$ (Banner et al. 2002). Several studies have since used either wave mean square slope or the azimuthal-integrated saturation spectrum to estimate breaking probabilities (Kleiss and Melville 2010; Gemmrich et al. 2008; Hwang et al. 2013). Following Banner et al. (2002), we calculate the average $\tilde{B}$ for frequency bands at and above the spectral peak using relative frequency bandwidths with center frequency f_c and bandwidths $f_c - \delta f_c \le f_c \le f_c + \delta f_c$, where δ was taken to be 0.15. The empirical angular spreading width formulation proposed by Hwang et al. (2000) was used in the calculation of $\tilde{B}$. This approach to estimating spectral breaking probabilities was shown to be insensitive to the value of δ by Banner et al. (2002).

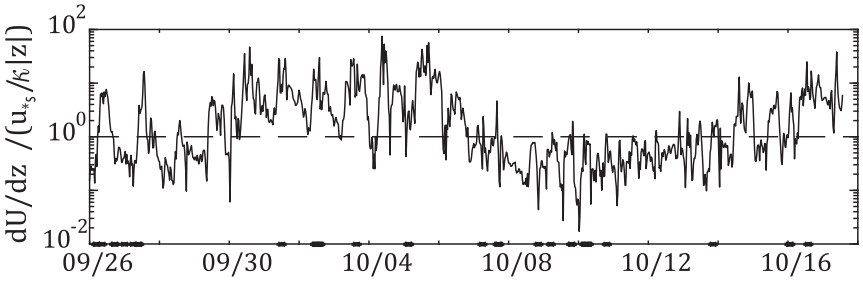

FIG. 2. Time series of Eulerian shear measured at $z \sim -2.5$ m normalized by surface log layer. During periods of active wind and wave forcing, the measured near-surface shear was much less than that expected for a surface log layer and was consistent with the conceptual model of a free shear transport layer used in scaling turbulent quantities beneath breaking waves. Black dots denote periods when the mean current was directed between 250° and 310°.

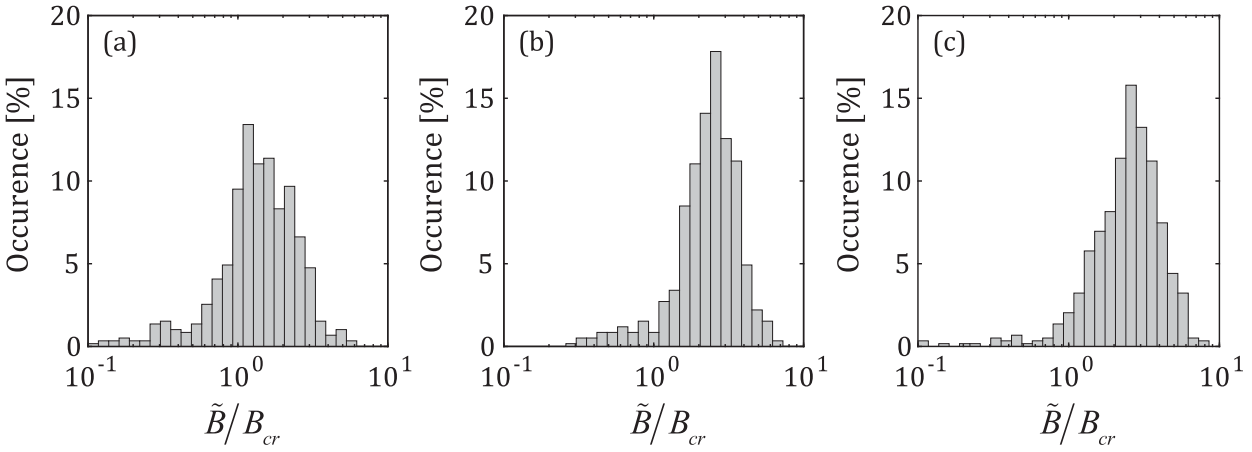

FIG. 3. Distributions of the average azimuthal-integrated spectral saturation $B(k)$, normalized by a common critical breaking threshold, for frequency-relative bandwidths corresponding to (a) $f_c/f_p = 1$, (b) $f_c/f_p = 1.35$, and (c) $fc/fp = 1.75$. Results indicate that breaking crests occurred at wave frequencies at and above the spectral peak during periods of strong wind and wave forcing at the tower site.

Results, shown in Fig. 3, indicate that the saturation spectrum observed at the tower site often exceeded the critical breaking threshold for frequencies at and above the spectral peak ($f = f_p$). The distributions of $\tilde{B}/B_{\mathrm{cr}}$ for $f_c/f_p = 1$ (Fig. 3a), $f_c/f_p = 1.35$ (Fig. 3b), and $f_c/f_p = 1.75$ (Fig. 3c) had mean values of 1.54 ± 0.89, 2.47 ± 1.19, and 2.67 ± 1.38, respectively. During the analysis period, wave crests frequently broke across a range of wave scales with values of $\tilde{B}/B_{\mathrm{cr}}$ exceeding unity approximately 72% ($f_c/f_p = 1$), 91% ($f_c/f_p = 1.35$), and 93% ($f_c/f_p = 1.75$) of the analysis period. During periods of strong wind and wave forcing, multiscale wave breaking likely occurred at the tower site, with breaking crests from a range of wave frequencies contributing to the turbulent fluxes measured by the tower ADVs.

Chesapeake Bay is a partially stratified estuary, in which stratification often suppresses vertical mixing. It is therefore informative to consider a framework used in describing turbulence in stratified flows before proceeding to an analysis of the effects of surface waves on turbulent quantities. Following a similar approach used in Stacey et al. (1999), we examine the data collected during this experiment within the turbulent state space suggested by Ivey and Imberger (1991). Results suggest that 1) Chesapeake Bay is considerably more energetic (turbulent Reynolds numbers Re_t ranging from 10^2 to 10^6) than the lake data (Re_t ranging from 10^1 to 10^4) analyzed in Ivey and Imberger (1991), consistent with previously reported observations of estuarine turbulence (e.g., Stacey et al. 1999); and 2) despite moderate wind forcing, a significant fraction of the data falls within the stratification-controlled regime discussed by Luketina and Imberger (1989) and Ivey and Imberger (1991). Persistent near-bottom stratification limited vertical mixing and likely capped the vertical extent of the bottom boundary layer with a number of near-bottom data falling at the transition between region II (stratification controlled) and region III (buoyancy suppressed) of the Ivey and Imberger (1991) state space. Because data in region III represents internal wave energy rather than active turbulence, all data for which the turbulence activity $\varepsilon/\nu N^2$ (where ν is the kinematic viscosity) was less than 20 (Itsweire et al. 1993; Stacey et al. 1999) was omitted from any further analysis (2% of the data).

b. TKE budget

As documented in numerous other studies (Agrawal et al. 1992; Anis and Moum 1995; Terray et al. 1996; Drennan et al. 1996; Greenan et al. 2001; Feddersen et al. 2007; Jones and Monismith 2008b), dissipation rates measured beneath breaking waves greatly exceeded wall layer scaling during this experiment. Within the wave-affected surface layer, elevated dissipation rates were balanced to first order by a divergence in the vertical transport of TKE, which was driven primarily by the pressure work associated with breaking-induced vorticity as discussed by Scully et al. (2016). This pressure work was more than an order of magnitude larger than the sum of the Eulerian and Stokes drift shear production and was a factor of 4 larger than the divergence in the vertical flux of TKE (Scully et al. 2016). Below the wave transport layer, dissipation was primarily balanced by shear production. For a more thorough analysis of the TKE budget observed during this experiment, including a discussion of the TKE transport driven by pressure work, see Scully et al. (2016).

During the experiment, energetic wave breaking (Scully et al. 2016) and Langmuir turbulence (Scully et al. 2015) were documented during periods of active

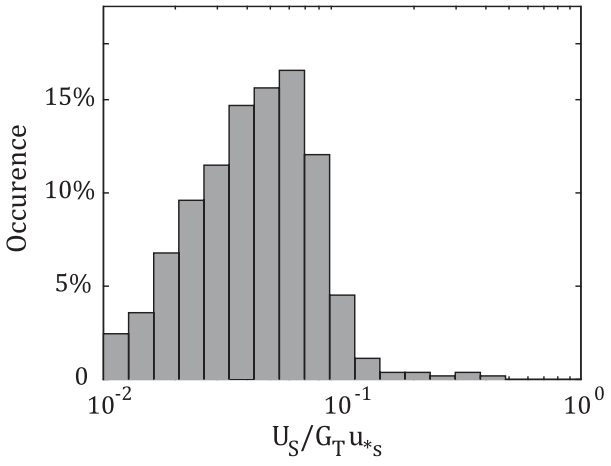

FIG. 4. Ratio of the surface TKE flux generated by the CL2 vortex force to the turbulent TKE flux generated by breaking waves. Wave breaking dominates the surface TKE flux with Langmuir turbulence contributing less than 10%.

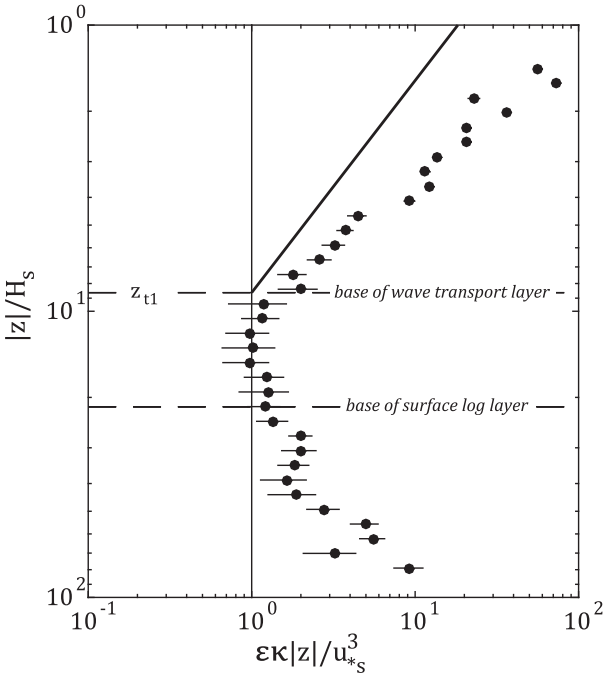

FIG. 5. Observed profile of dissipation normalized by log layer scaling [Eq. (3)]. Horizontal dotted lines represent transition depths between the wave transport layer, surface log layer, and bottom boundary layer. The average depth of the transition between the wave transport layer and the surface log layer agrees well with the analytical scaling in Eq. (18). Solid black line represents Terray et al. (1996) scaling for a wave transport layer.

wave forcing. Because wave breaking can provide a seed of vertical vorticity that generates Langmuir turbulence through the CL2 vortex force mechanism (Craik and Leibovich 1976; Leibovich 1983), it is informative to quantify the relative contributions of Langmuir turbulence and wave breaking to the surface TKE flux. Skyllingstad and Denbo (1995) suggest that the turbulent TKE flux generated by the CL2 vortex force should scale with $U_S u_{*_s}^2$, where U_S is the surface Stokes drift. Following Jones and Monismith (2008a) and using Eq. (15), the ratio of turbulent TKE flux generated by Langmuir turbulence to the turbulent TKE flux generated by breaking waves within the wave transport layer can then be expressed as $U_S/G_T u_{*_s}$.

During the course of the experiment, wave breaking was the dominant source of TKE in the wave transport layer with Langmuir turbulence contributing less than 10% of the surface TKE flux (Fig. 4). This is similar to the results presented by Jones and Monismith (2008a) for a shallow estuarine environment in Grizzly Bay, California, and consistent with the results of Scully et al. (2016) in which the Stokes production term was found to be insignificant compared to the divergence in the turbulent TKE flux driven by the pressure work under breaking waves. The Skyllingstad and Denbo (1995) relation does not, however, describe the effects of Stokes drift shear in modifying vertical transport regimes within the wave transport layer.

c. *Dissipation structure and scaling*

The depth at which the wave transport layer transitions to a surface log layer can be found by equating the scaling arguments for a wave transport layer [Eq. (2)] and a surface log layer [Eq. (3)] (Terray et al. 1996; Jones and Monismith 2008a):

$$z_{t1} = -0.3kH_S G_T. \tag{18}$$

The base of the wave transport layer occurs at z_{t1} and represents the point at which the surface TKE flux generated by breaking waves becomes negligible relative to local shear production. The observed dissipation profile, scaled by surface log layer scaling, is presented in Fig. 5. Note that the nondimensional depth $|z|/H_S$ used to bin average results accounts for variability in wave height and water level changes due to tides and wind-driven setup. The analytical mean transition depth between the wave transport layer and the surface log layer is shown as a horizontal dotted line.

Within the wave transport layer, dissipation estimates generally agree with the canonical model of Terray et al. (1996), but are elevated relative to Terray et al. (1996) scaling [Eq. (2); thick black line in Fig. 5]. The transition between wave transport layer and surface log layer occurs at $z_{t1} = -4.94 \pm 0.09$ m. While measured dissipation rates exceeded the scaling suggested by Terray et al. (1996) within the wave transport layer, the transition

to a surface log layer occurred at the same depth as predicted by Eq. (18).

Thomson et al. (2016) showed that the choice of reference frame can significantly impact the apparent depth of elevated dissipation rates. Because turbulence generated by wave breaking often persists over multiple wave periods (Sullivan et al. 2004), it will be carried down to trough level by wave orbital velocities yet appear isolated to a shallow near-surface region in fixed reference frames (Thomson et al. 2016). As a result, studies that use a reference frame relative to the mean free surface (Terray et al. 1996; Drennan et al. 1996; Feddersen 2012) often report high dissipation values deeper than studies that use a wave-following reference frame (Gemmrich 2010; Thomson 2012; Sutherland and Melville 2015; Zippel and Thomson 2015; Thomson et al. 2016). The fixed reference frame used in this study may, therefore, lead to elevated dissipation rates deeper in the water column, but the qualitative structure of the observed turbulent profiles and the evaluation of turbulence closure assumptions (section 5) is robust.

In an estuarine environment like Chesapeake Bay, the bottom boundary layer is tidally dominated while the surface boundary layer is wind dominated. Based on comparison to expected surface log layer scaling, Fig. 5 demonstrates that the surface log layer extended to a depth of $\sim 8.40 \pm 0.12$ m. The gradient Richardson number often exceeded the critical value of 0.25 near the seabed, suggesting that the height of the bottom boundary layer was restricted by stable stratification. Characterizing the specific nature of the stratified bottom boundary layer observed during this experiment, however, is beyond the scope of this paper.

The challenges and limitations associated with measuring turbulent dissipation in situ means that observations of a multilayer turbulent response to wind forcing are rare despite being predicted by the analytical solutions of Craig and Banner (1994), Craig (1996), Terray et al. (1996), and Burchard (2001). A three-layer structure—consisting of a wave transport layer, a surface log layer, and a stratified bottom boundary layer—dominated the wind-forced response at the tower site with the depth of the wave transport layer being shallower than the depth of the surface log layer for 98% of the observations.

Scully et al. (2016) documented that negative pressure skewness associated with TKE transport driven by pressure work was limited to depths shallower than $z = -0.2\lambda$, where λ is the wavelength associated with H_S, which is consistent with the laboratory results of Melville et al. (2002) for the maximum depth of penetration of roll vortices generated by breaking waves. The ratio of the observed z_{t1} to -0.2λ is shown in Fig. 6. The distribution of $|z_{t1}|/0.2\lambda$ had a mean of 1.4, suggesting that coherent breaking-induced vortices occupied a significant fraction of the wave transport layer and that the wave transport layer extended below the maximum depth of penetration of breaking waves observed during this experiment.

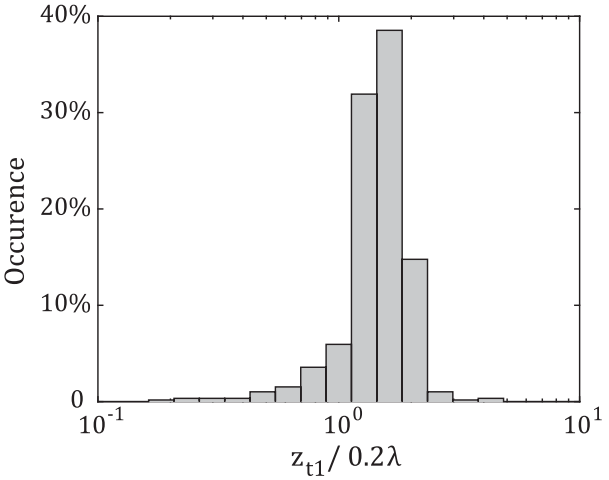

FIG. 6. Distribution of the ratio of the wave transport layer depth z_{t1} to the expected maximum depth of breaking-induced roll vortices (Melville et al. 2002, Scully et al. 2016). The mean of the distribution is approximately 1.4, which suggests that the depth of the wave transport layer exceeded the maximum depth of penetration of breaking waves.

d. *Relationship between turbulent length scale, dissipation, and TKE*

The relation between dissipation, TKE, and the turbulent length scale [Eq. (10)] can be used to evaluate the relationship between the stability function and turbulent length scale used in second-moment closure schemes. Following Umlauf and Burchard (2003), we may assume that the turbulent length scale increases linearly with distance from the boundary such that

$$l = L|z|, \tag{19}$$

where L is typically taken as a constant. In an unstratified log layer $L = \kappa = 0.41$. In a transport layer, however, L is expected to decrease based on grid stirring experiments and direct numerical simulations of free shear turbulence (Umlauf and Burchard 2003). The modeling experiments of Umlauf and Burchard (2003) suggest that $L \sim 0.2$ for wave breaking transport modeled as a free shear layer, but field observations that validate this assumption are rare. Jones and Monismith (2008b) found that $L = 0.25$ was needed to reproduce dissipation rates measured within the wave transport layer using a one-equation closure model with a constant stability function and $z_0 = O(H_S)$.

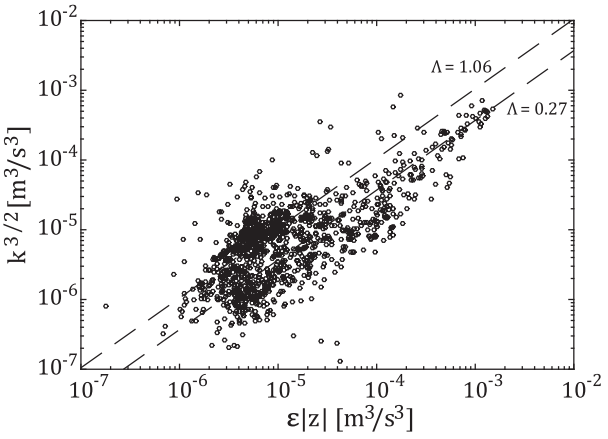

FIG. 7. Relationship between TKE, dissipation, and the turbulent length scale observed at upper two ADVs ($z \sim -1.7$ and -3.5 m). The solid black line represents a linear regression line that yields a Λ value [Eq. (20)] of 1.06. The dashed line denotes a Λ value associated with the largest dissipation events ($\Lambda = 0.27$).

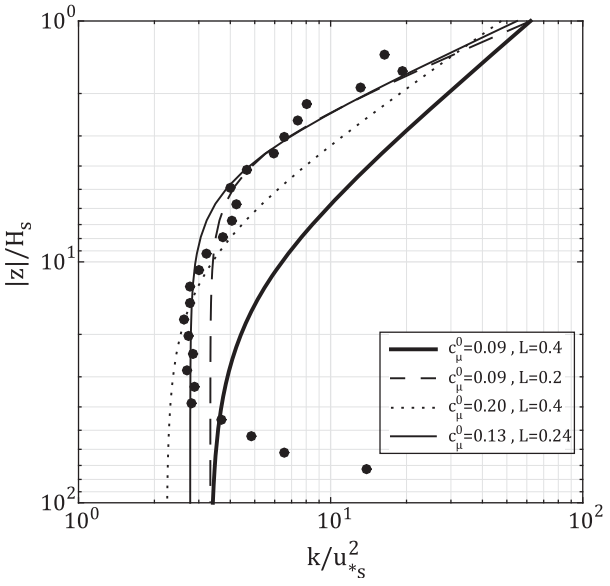

FIG. 8. Comparison of the observed TKE profile to analytic solutions [Eq. (21)] of Craig (1996), Burchard (2001), and Gerbi et al. (2009). Rigid-wall scaling is shown as a thick solid black line. Fits proposed by Gerbi et al. (2009) for the CBLAST-LOW dataset are shown as dashed and dotted lines. The thin solid black line is a best-fit curve to our dataset using an observed Λ value of 1.06, which corresponds to a constant stability function of $c_\mu^0 = 0.13$ and $L = 0.24$.

Combining Eq. (10) with Eq. (19), we can evaluate the relation between stability function and length scale growth rate directly using measurements of dissipation and TKE (Gerbi et al. 2009):

$$k^{3/2} = \frac{L}{c_\mu^{0(3/4)}}\varepsilon|z| = \Lambda\varepsilon|z|, \tag{20}$$

where $\Lambda = L/c_\mu^{0(3/4)}$. Gerbi et al. (2009) showed that near-surface dissipation and TKE observations collected as part of the Coupled Boundary Layers Air-Sea Transfer Low Wind Component (CBLAST-LOW) experiment suggest that Λ is significantly reduced in the wave transport layer when compared to rigid boundary scaling derived using $L = \kappa$ and $c_\mu^0 = 0.09$.

In Fig. 7, a scatterplot of TKE and dissipation measured at the top two ADVs ($z \sim -1.7$ m and $z \sim -3.5$ m) is shown. A linear regression of the data yields a Λ of 1.06, which is consistent with the value reported by Gerbi et al. (2009) for the CBLAST-LOW experiment. Assuming a constant stability function, this is consistent with the reduction in length scale relative to rigid boundary scaling that has been reported by previous studies. During large dissipation events, Λ is significantly reduced (0.27), suggesting that either the turbulent length scale is greatly reduced under energetic breaking conditions or that the stability function value is greatly enhanced.

e. *Vertical profile of TKE*

Craig (1996) developed an analytical solution for the vertical profile of TKE in the oceanic surface layer through solution of the TKE equation invoking a balance between dissipation, shear production, and vertical divergence of TKE transport. The model was shown to be consistent with the predictions from a full k–ε model (Burchard 2001) and has been used to compare observed energy profiles with model predictions (Gerbi et al. 2009; Li et al. 2013). Following the notation of Gerbi et al. (2009), the Craig (1996) model for TKE can be expressed as follows:

$$\frac{k^{3/2}}{u_{*_s}^3} = \frac{1}{c_\mu^{0(3/4)}} + G_b\left(\frac{3\sigma_k}{2c_\mu}\right)^{1/2}\left(\left|\frac{z}{z_o}\right|\right)^{-m}, \tag{21}$$

where

$$m = \frac{1}{\Lambda}\left(\frac{3\sigma_k}{2c_\mu}\right)^{1/2}. \tag{22}$$

The $G_b u_{*_s}^3$ is the turbulent TKE flux into the wave transport layer and σ_k is the turbulent Schmidt number. The first term on the right-hand side is the log layer limit (production dominant), and the second term is the wave transport layer limit (divergent TKE transport dominates). It should be noted that the Gerbi et al. (2009) form of the Craig (1996) model accounts for a virtual origin at the base of the wave breaking layer as suggested by Burchard (2001) and maintains the distinction between the stability function used in the calculation of the eddy viscosity c_μ

and a constant stability function assumed for the surface log layer (unstratified; $c_\mu = c_\mu^0 = 0.09$).

We compare the observed TKE profile to the one-equation model of Craig (1996) using $z_0 = -H_S$ and by assuming that $\sigma_k = 1$ in Fig. 8. Following Burchard (2001) and Gerbi et al. (2009), we assume that $c_\mu = c_\mu^0$, such that the values of c_μ^0 and L of are constrained by Λ. Furthermore, using the results discussed in section 3d, we evaluate the model for values of c_μ^0 and L that are equivalent to the observed Λ value of 1.06. The observed TKE profile and model predictions for $\Lambda = 1.06$ are shown in Fig. 8, along with curves suggested for the CBLAST-LOW experiment and for rigid-boundary scaling (Gerbi et al. 2009). The model agrees well with our data when evaluated with a c_μ^0 value of 0.13 and $L = 0.24$ and captures the transition from a wave transport layer to a surface log layer that occurs at $z \sim -10H_S$. Increasing TKE near the bed is indicative of the bottom boundary layer, which is not accounted for in the Craig (1996) model. A value of $L = 0.24$ is consistent with the findings of Jones and Monismith (2008b) and the proposed transport layer scaling of Umlauf and Burchard (2003); however, Λ values in our data were significantly lower during large dissipation events suggesting that L and/or c_μ^0 were not constant within the wave transport layer.

Because of uncertainty regarding the proper value of z_0 (Terray et al. 1996; Burchard 2001; Umlauf and Burchard 2003; Jones and Monismith 2008b; Gerbi et al. 2009), we briefly discuss the implications of using a constant value of $z = O(-H_S)$ in Eq. (21). Recent observations have shown that the highest turbulent dissipation rates occur very near the surface (Gemmrich 2010; Thomson 2012; Sutherland and Melville 2015; Thomson et al. 2016), which is much shallower than the constant dissipation layer hypothesized by Terray et al. (1996) ($z_0 = 0.6H_S$). The choice of z_0 is further complicated when multiscale breaking occurs, when breaking crests may inject turbulence at a range of depths and turbulence generated by small breakers may be advected downward by larger breakers (Sutherland and Melville 2015). This suggests that it is unlikely that a constant value of z_0 is appropriate for a realistic wind sea.

The shallowest measurements presented here only extend to slightly deeper than $z = -H_S$, so direct estimates of z_0 from this dataset are not possible. Using a constant value of $z = -H_S$ in Eq. (21) represents a plausible upper bound on the depth of the active breaking layer, shifting the modeled profile of TKE deeper in the water column, and therefore affecting the constant values of c_μ^0 and L used in fitting the profile to the data. In addition to the uncertainty in z_0, the applicability of $\sigma_k = 1$ to turbulence generated beneath breaking waves also remains a matter of debate. While the Craig (1996) model can be tuned to accurately reproduce the observed turbulent kinetic energy profile, variability in Λ indicates that more complex modeling methods are likely needed to accurately simulate turbulent fluxes under breaking waves.

5. Discussion

The results presented in the previous section indicate that while one-dimensional closure models can be tuned to reasonably reproduce the mean profiles of dissipation and TKE, accurately modeling the vertical momentum flux likely requires a more complex approach. In the following discussion, we compare observations to predicted values of the stability function used in second-moment turbulence closures and evaluate the importance of nonlocal turbulent transport beneath breaking waves.

a. Observed versus predicted stability functions

Following Scully et al. (2011), the value of the stability function can be estimated from Eqs. (5) and (8) using observations of TKE, dissipation, stress, and shear: $c_\mu = A_z\varepsilon/k^2 = -\langle u'w'\rangle\varepsilon/(Sk^2)$. Measurements of stress, TKE, and dissipation were linearly interpolated between ADV sensor heads to give estimates collocated with shear. The momentum flux vector measured in the wave transport layer during this experiment was aligned with the mean direction of the Lagrangian shear suggesting that Stokes drift likely altered vertical transport regimes (Fisher et al. 2017). We therefore chose to calculate the eddy viscosity from the mean Lagrangian shear, $-\langle u'w'\rangle = A_z(\partial U_i/\partial z + \partial U_{Si}/\partial z)$, to account for the observed wave-aligned marine stress vector (Scully et al. 2016; Fisher et al. 2017).

To assess the performance of stability functions commonly employed in second-moment closure schemes, we compare observed stability function values to those predicted by the quasi-equilibrium formulation of Kantha and Clayson 1994 (hereinafter KC94) and the nonequilibrium formulations of KC94 derived by BB01 and CA01. For a detailed discussion of these functions, see BB01. Stability function values predicted by KC94, BB01, and CA01 were calculated using observed profiles of the momentum flux, mean Lagrangian shear, dissipation, buoyancy frequency, and TKE.

Predicted and observed stability function values, bin averaged by mean depth, are shown in Fig. 9. A constant stability function value does not represent this dataset well as observed stability function values ranged over two orders of magnitude. While all three models reasonably reproduce low stability function values observed in the region of the water column where shear production dominated and stable stratification limited turbulent length scales, the models significantly underpredict large observed stability function values within the wave

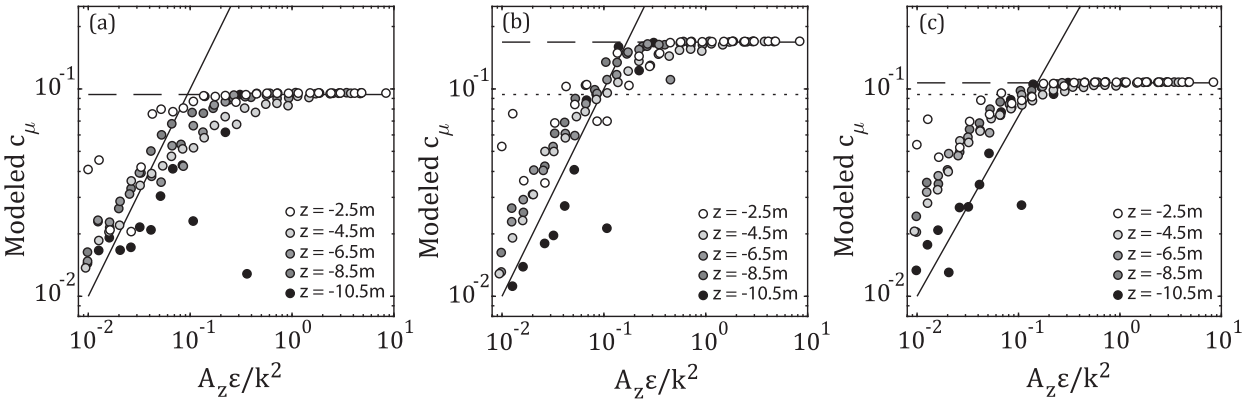

FIG. 9. Bin-averaged comparison of predicted stability functions and observed stability functions. (a) KC94, (b) KC94 rederived by BB01, and (c) CA01. Dashed lines are empirical asymptotes in free shear conditions and dotted lines represent the value of c_μ^0. In the wave-affected surface layer, observed stability functions greatly exceed empirical asymptotes and can be $O(1)$.

transport layer. Within the wave transport layer, results indicate that observed c_μ values ranged from $O(10^{-2})$ to $O(1)$ with a mean value of 0.42, which significantly exceeds free shear limits often employed in closure schemes (Umlauf and Burchard 2003). The asymptotic free shear limits of KC94, BB01, and CA01 are ~0.09, ~0.17, and ~0.11, respectively (shown as dashed lines in Fig. 9). The nonequilibrium formulation of BB01 produces less scatter and performs slightly better than CA01 when compared to observations. The observed underprediction of the stability function within the wave transport layer is likely rooted in the fact that grid-stirring experiments are commonly used to calibrate stability functions for free shear conditions, which produce a near-constant source of TKE versus intermittent energetic injections of energy under breaking waves and do not account for the enhanced vertical transport scales due to Langmuir turbulence and/or coherent wave-breaking vortices.

Using observed Λ and stability function values in Eq. (20) yields an average $L = 0.20$, which is consistent (though slightly smaller) with the model fit for the TKE profile presented in Fig. 8 and the modeling results of Umlauf and Burchard (2003). This indicates that within the wave transport layer, the vertical transport of TKE is carried out by eddies smaller than those responsible for shear production next to a rigid boundary.

Because the only difference between predicted and observed eddy viscosities was the value of the stability function, a comparison of predicted eddy viscosity to observed eddy viscosity (Fig. 10) demonstrates the impact of underpredicting the value of the stability function in the wave transport layer. A logarithmic regression of predicted versus observed values of the eddy viscosity indicates that the higher-level closure solutions of the two nonequilibrium formulations of BB01 (slope = 0.70; $R^2 = 0.83$) and CA01 (slope = 0.55; $R^2 = 0.61$) performed better than the quasi-equilibrium formulation of KC94 (slope = 0.28; $R^2 = 0.39$). Using the KC94 stability function resulted in a large underprediction of eddy viscosity near the surface and an overprediction of the eddy viscosity in stratified conditions deeper in the water column. Both CA01 and BB01 showed strong agreement for $|z| > 7H_S$ where stable stratification limited turbulent length scales and shear production became more dominant. However, both nonequilibrium formulations underpredict (by nearly an

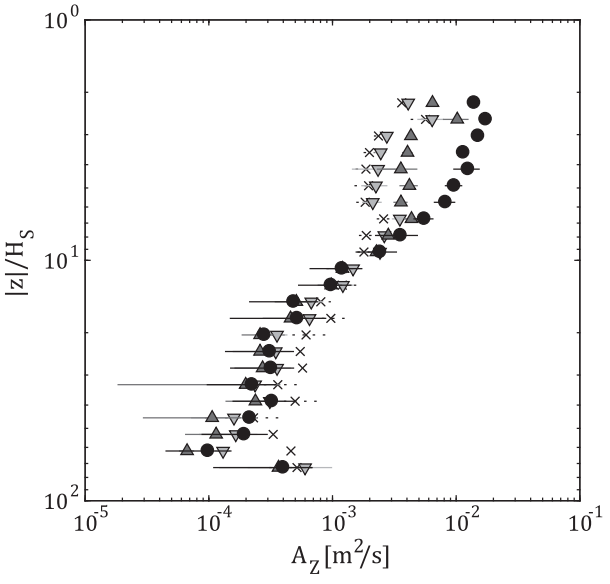

FIG. 10. Comparison of modeled [BB01 (dark gray), CA01 (light gray), and KC94 (black x's)] and observed (black circles) profiles of eddy viscosity shown with standard error bars. The asymptotic behavior of predicted stability functions results in a significant underprediction of eddy viscosity in the wave-affected surface layer.

order of magnitude) the eddy viscosity observed under breaking waves. This indicates that the presence of breaking waves homogenized the surface mixed layer to a greater extent than predicted by the classical model of TKE diffusing away from a source at the surface.

b. *Influence of nonlocal momentum and TKE transport*

The intermittency of breaking crests at the ocean surface (Sutherland and Melville 2015) suggests that the transport of momentum and mechanical energy within the oceanic surface boundary layer may be fundamentally different than the downgradient (e.g., eddy diffusivity) formulation employed in most second-moment turbulence closure schemes [Eq. (5)]. A simple test of the validity of the downgradient assumption used in second-moment turbulence closures is to compare measured turbulent fluxes to measured vertical gradients.

The results for the turbulent transport of TKE, shown in Fig. 11, indicate that the total turbulent TKE flux was largely downgradient when TKE decreased away from the surface (88% of the analysis period). A logarithmic regression of the total TKE flux and the vertical gradient in TKE yielded a slope of 0.87 and an R^2 value of 0.60 for periods when the total TKE flux was directed downgradient. Despite clear differences between the grid-stirring experiments used to tune closure models and the intermittent nature of oceanic wave breaking, second-moment turbulence closures have been used to reproduce measured profiles of dissipation with reasonable accuracy (Burchard 2001, Umlauf and Burchard 2005). The modeling results of Melsom and Sætra (2004) suggest that shear production is only important episodically during breaking events, which provides a conceptual link between diffusive breaking models and realistic wave breaking (Umlauf and Burchard 2005). The significant trend shown in Fig. 11 supports an eddy diffusivity model of the turbulent transport of TKE beneath breaking waves; however, the specific value of the turbulent Schmidt number and dependence on the eddy viscosity remain open scientific questions.

In contrast, the turbulent momentum flux exhibits no clear trend with local mean shear in the wave transport layer. Conceptually, breaking crests episodically inject momentum and energy to the water column during strong downward "sweeps" of high velocity fluid that coincide with negative vertical velocities consistent with the results of Scully et al. (2016). Observations of the momentum flux generated principally by intermittent breaking events were largely independent of the mean shear, which was very low near the surface (Fig. 2). However, the direction of stress within the wave transport layer was observed to be coaligned with the direction of the Lagrangian shear during

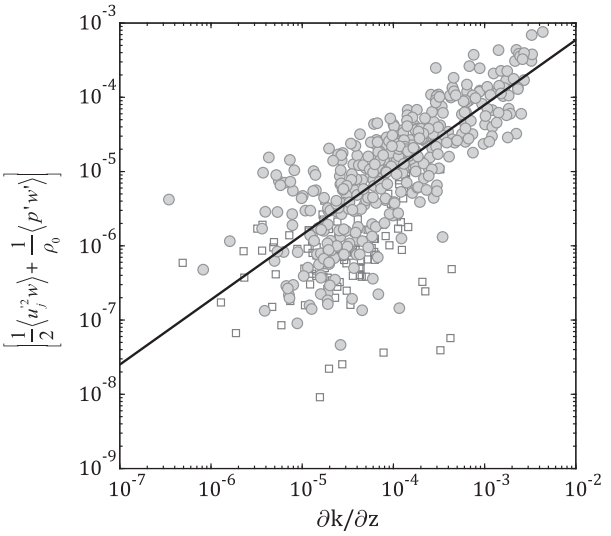

FIG. 11. Observed total turbulent TKE flux vs the vertical gradient of TKE. Gray circles are periods when the TKE flux was directed downgradient and white squares are periods when it was countergradient. Black line is a logarithmic regression of the downgradient TKE flux ($R^2 = 0.60$).

this experiment (Fisher et al. 2017), which suggests that the total shear generated by the mean flow and the surface wave field likely played an important role, at least transiently, in transferring the momentum generated by surface wave energy dissipation to a momentum flux within the water column. A possible explanation for the discrepancy between these results is the turbulent transport of a nonlocal momentum flux by coherent large-scale turbulent eddies.

Most models predict that the ratio of stress to TKE should decrease with increasing density stratification and when dissipation exceeds the sum of shear and buoyancy production (Scully et al. 2011). By Eq. (13), as the ratio of shear production to dissipation decreases so should the value of the nondimensional stress. Because buoyancy production of TKE was insignificant in this dataset (Scully et al. 2016), the nondimensional stress provides a useful framework for evaluating the influence of nonlocal turbulent transport in structuring the profile of stress in the water column. In Fig. 12, the observed profile of $-\langle u'w'\rangle/k$ is compared to predicted values of nondimensional stress using Eq. (13) and the BB01 stability function.

A key difference between these two profiles is the eddy viscosity assumption employed in the second-moment closure predictions. Both profiles decrease toward the surface where dissipation is balanced by a vertical divergence in total TKE flux and converge on a constant value (much lower than typically assumed for a neutral log layer) near the bed where significant stable

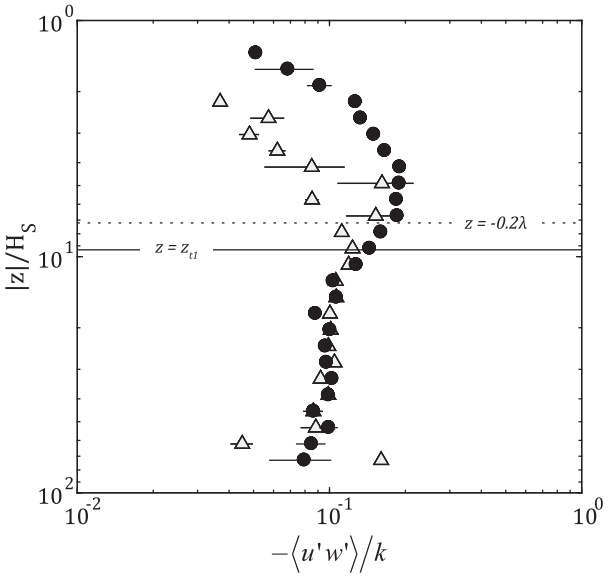

FIG. 12. Comparison of the observed nondimensional stress profile (black) to the predictions of a second-moment closure using BB01 (light gray). Solid black line indicates the depth of the wave transport layer, and the dotted black line denotes the maximum depth of negative pressure skewness observed by Scully et al. (2016).

stratification existed. However, within the wave transport layer, the observed ratio of stress to TKE greatly exceeded predicted values. Furthermore, a subsurface maximum in the observations is opposite of what is expected for a transport layer in which the ratio of P/ε should increase with depth—a result predicted by the nonequilibrium stability function of BB01 shown in Fig. 12. The location of the subsurface maxima in the observed nondimensional stress corresponds to the maximum depth of penetration role vortices suggested by Melville et al. (2002) and the maximum depth of negative pressure skewness measured by the tower ADVs (Scully et al. 2016). The underprediction of the stability function in the wave transport layer is, therefore, likely due to the turbulent transport of the momentum flux being modeled as a downgradient process in the formulation of second-moment closures. It is quite likely that nonlocal momentum fluxes contribute significantly in environments characterized by episodic wave breaking and coherent turbulent structures and that the turbulent transport of that momentum occurs largely in the absence of mean shear.

Conditional averaging of ADV burst data indicates that TKE transport carried out by pressure work associated with breaker roll vortices was associated with upward vertical velocities while the momentum flux was associated with downward sweeps of high velocity fluid (Scully et al. 2016). This suggests that the momentum flux and the TKE transport may have been carried out by different classes of turbulent eddies within the wave transport layer. A sample time series of the instantaneous momentum flux and pressure work observed at the uppermost ADV shows apparent independent sweeps of high momentum fluid that were unaccompanied by an instantaneous spike in pressure work (Fig. 13). Two significant downward sweeps of momentum occurred early in the record that did not have a corresponding breaking eddy signature (e.g., spike in pressure work). Rapp and Melville (1990) demonstrated that as much as 25% of the total air–sea momentum flux could be attributed to plunging breaker events, but the laboratory experiments of Melville et al. (2002) showed that despite breaker roll vortices reaching depths of $z = -0.2\lambda$, the momentum flux associated with breaking impulses was quite small.

The results shown in Figs. 12 and 13 suggest that the vertical turbulent transport of TKE and momentum may have been carried out by different classes of turbulent eddies, consistent with the cospectral analysis shown by Scully et al. (2016). Conducting simulations for a range of breaking intensities, Sullivan et al. (2007) determined that energetic breaking reduced the coherency of Langmuir cells. Energetic breaking events disrupted Langmuir turbulence and resulted in strong, localized downwelling jets that were strained by the CL2 vortex force into a patchy distribution of intensified vertical vorticity (Sullivan et al. 2007). This picture is consistent with the observations presented here, where strong fetch-limitation resulted in the multiscale wave breaking that transferred energy from the wave field to TKE primarily through pressure work (Scully et al. 2016) and momentum generated near the surface was transported downward by larger-scale coherent turbulent motions, such that the direction of stress in the wave transport layer was coaligned with the direction of Lagrangian shear (Fisher et al. 2017).

6. Conclusions

Direct observations of dissipation, TKE, and stress indicate that breaking waves dominated the structure of turbulent transport within the oceanic surface boundary layer of Chesapeake Bay. During periods of active wave forcing, a three-layer turbulent response was detected in which the wave transport layer transitioned to a surface log layer ($z \sim -10H_S$), which then merged with the tidal, bottom boundary layer. The depth of the transition between the wave transport layer and the surface log layer agreed well with the analytical scalings suggested by Terray et al. (1996) and Jones and Monismith (2008a).

Within the wave transport layer, elevated dissipation rates were balanced by a vertical divergence in the total

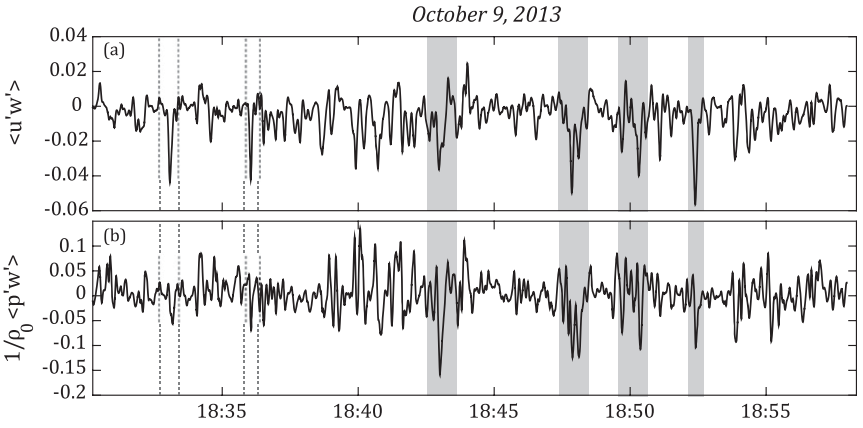

FIG. 13. Sample plot of the (a) instantaneous momentum flux and (b) pressure work observed on 9 Oct 2013. Shaded regions represent periods of strong correlation between TKE transport and momentum flux, while dashed lines indicate periods when downward momentum sweeps occur without a corresponding breaking eddy signature.

TKE transport. Breaking waves dominated the TKE budget within the wave-affected surface layer contributing over 90% of the surface TKE flux. As assumed in most closure models, the dissipation rate and TKE were related through a length scale proportional to the distance from the surface boundary. However, this proportionality coefficient was determined to be less than half that expected for turbulence produced near a rigid boundary and was not constant during the experiment. A comparison of the base of the wave transport layer to the maximum depth of negative pressure skewness, which corresponded to energetic breaking events (Scully et al. 2016), indicates that the wave transport layer extended below the maximum depth of roll vortices generated beneath breaking waves.

The one-equation closure model of Craig (1996) model, modified by Burchard (2001) and Gerbi et al. (2009), agreed well with the measured average profile of TKE when applied using a constant $z_0 = -H_S$, stability function value of $c_\mu^0 = 0.13$, and surface length scale growth rate of $L = 0.24$. However, stability function values calculated from time series of observed TKE, stress, shear, and dissipation ranged over two orders of magnitude and greatly exceeded the maximum values of nonequilibrium and quasi-equilibrium formulations of the stability function within the wave transport layer. As a result, modeled values significantly underpredicted observed eddy viscosities in the wave transport layer. Within the buoyancy-controlled interior, both nonequilibirum parameterizations performed well and accurately predicted observed mixing profiles. Both nonequilibrium stability functions performed better than the quasi-equilibrium function within the wave transport layer and in regions of significant stratification.

The vertical divergence of turbulent TKE transport was found to occur downgradient of the observed profile of TKE in the wave transport layer, supporting the use of eddy diffusivity models used in second-moment closures to parameterize turbulent transport terms. However, the momentum flux was not significantly correlated with the mean shear, despite the Reynolds stress being aligned with the direction of mean Lagrangian shear within the surface layer of the estuary. The observed ratio of stress to TKE suggests that turbulent transport of a nonlocal momentum flux, generated near the surface, by large coherent turbulent eddies likely played a role in structuring momentum exchange within the wave transport layer. This in combination with analysis of the instantaneous momentum flux and pressure work suggests that the momentum flux and turbulent TKE flux were likely carried out by different classes of turbulent eddies.

The transfer of momentum and mechanical energy beneath breaking waves has important implications for mixing in the coastal ocean. Underpredictions of the eddy viscosity within the surface layer suggest that current modeling efforts could benefit from further research into the form and nature of turbulent transport carried out by coherent structures beneath breaking waves.

Acknowledgments. This manuscript benefited greatly from the comments and suggestions of two anonymous reviewers. This work was supported by National Science Foundation Grants OCE-1061609 and OCE-1339032.

REFERENCES

Agrawal, Y. C., E. A. Terray, M. A. Donelan, P. A. Hwang, A. J. Williams, W. M. Drennan, K. K. Kahma, and S. A. Kitaigorodskii, 1992: Enhanced dissipation of kinetic energy beneath surface waves. *Nature*, **359**, 219–220, https://doi.org/10.1038/359219a0.

Anis, A., and J. N. Moum, 1992: The superadiabatic surface layer of the ocean during convection. *J. Phys. Oceanogr.*, **22**, 1221–1227, https://doi.org/10.1175/1520-0485(1992)022<1221:TSSLOT>2.0.CO;2.

——, and ——, 1995: Surface wave–turbulence interactions: Scaling $\epsilon(z)$ near the sea surface. *J. Phys. Oceanogr.*, **25**, 2025–2045, https://doi.org/10.1175/1520-0485(1995)025<2025:SWISNT>2.0.CO;2.

Banner, M. L., J. R. Gemmrich, and D. M. Farmer, 2002: Multiscale measurements of ocean wave breaking probability. *J. Phys. Oceanogr.*, **32**, 3364–3375, https://doi.org/10.1175/1520-0485(2002)032<3364:MMOOWB>2.0.CO;2.

Burchard, H., 2001: Simulating the wave-enhanced layer under breaking surface waves with two-equation turbulence models. *J. Phys. Oceanogr.*, **31**, 3133–3145, https://doi.org/10.1175/1520-0485(2001)031<3133:STWELU>2.0.CO;2.

——, and K. Bolding, 2001: Comparative analysis of four second-moment turbulence closure models for the oceanic mixed layer. *J. Phys. Oceanogr.*, **31**, 1943–1968, https://doi.org/10.1175/1520-0485(2001)031<1943:CAOFSM>2.0.CO;2.

——, O. Petersen, and T. P. Rippeth, 1998: Comparing the performance of the Mellor–Yamada and the k–ϵ two-equation turbulence models. *J. Geophys. Res.*, **103**, 10 543–10 554, https://doi.org/10.1029/98JC00261.

Canuto, V. M., A. Howard, Y. Cheng, and M. S. Dubovikov, 2001: Ocean turbulence. Part I: One-point closure model—Momentum and heat vertical diffusivities. *J. Phys. Oceanogr.*, **31**, 1413–1426, https://doi.org/10.1175/1520-0485(2001)031<1413:OTPIOP>2.0.CO;2.

Chen, C., H. Liu, and R. C. Beardsley, 2003: An unstructured grid, finite-volume, three-dimensional, primitive equations ocean model: Application to coastal ocean and estuaries. *J. Atmos. Oceanic Technol.*, **20**, 159–186, https://doi.org/10.1175/1520-0426(2003)020<0159:AUGFVT>2.0.CO;2.

Chen, S. N., and L. P. Sanford, 2009: Axial wind effects on stratification and longitudinal salt transport in an idealized, partially mixed estuary. *J. Phys. Oceanogr.*, **39**, 1905–1920, https://doi.org/10.1175/2009JPO4016.1.

——, ——, and D. K. Ralston, 2009: Lateral circulation and sediment transport driven by axial winds in an idealized, partially mixed estuary. *J. Geophys. Res.*, **114**, C12006, https://doi.org/10.1029/2008JC005014.

Craig, P. D., 1996: Velocity profiles and surface roughness under breaking waves. *J. Geophys. Res.*, **101**, 1265–1277, https://doi.org/10.1029/95JC03220.

——, and M. L. Banner, 1994: Modeling wave-enhanced turbulence in the ocean surface layer. *J. Phys. Oceanogr.*, **24**, 2546–2559, https://doi.org/10.1175/1520-0485(1994)024<2546:MWETIT>2.0.CO;2.

Craik, A. D. D., and S. Leibovich, 1976: A rational model for Langmuir circulations. *J. Fluid Mech.*, **73**, 401–426, https://doi.org/10.1017/S0022112076001420.

Drennan, W. M., M. A. Donelan, E. A. Terray, and K. B. Katsaros, 1996: Oceanic turbulence dissipation measurements in SWADE. *J. Phys. Oceanogr.*, **26**, 808–815, https://doi.org/10.1175/1520-0485(1996)026<0808:OTDMIS>2.0.CO;2.

Elliott, J. A., 1972: Instrumentation for measuring static pressure fluctuations within the atmospheric boundary layer. *Bound.-Layer Meteor.*, **2**, 476–495, https://doi.org/10.1007/BF00821550.

Feddersen, F., 2012: Observations of the surf-zone turbulent dissipation rate. *J. Phys. Oceanogr.*, **42**, 386–399, https://doi.org/10.1175/JPO-D-11-082.1.

——, J. H. Trowbridge, and A. J. Williams, 2007: Vertical structure of dissipation in the nearshore. *J. Phys. Oceanogr.*, **37**, 1764–1777, https://doi.org/10.1175/JPO3098.1.

Fisher, A. W., L. P. Sanford, and S. E. Suttles, 2015: Wind stress dynamics in Chesapeake Bay: Spatiotemporal variability and wave dependence in a fetch-limited environment. *J. Phys. Oceanogr.*, **45**, 2679–2696, https://doi.org/10.1175/JPO-D-15-0004.1.

——, ——, M. E. Scully, and S. E. Suttles, 2017: Surface wave effects on the translation of wind stress across the air–sea interface in a fetch-limited, coastal embayment. *J. Phys. Oceanogr.*, **47**, 1921–1939, https://doi.org/10.1175/JPO-D-16-0146.1.

Gemmrich, J. R., 2010: Strong turbulence in the wave crest region. *J. Phys. Oceanogr.*, **40**, 583–595, https://doi.org/10.1175/2009JPO4179.1.

——, and D. M. Farmer, 1999: Observations of the scale and occurrence of breaking surface waves. *J. Phys. Oceanogr.*, **29**, 2595–2606, https://doi.org/10.1175/1520-0485(1999)029<2595:OOTSAO>2.0.CO;2.

——, and ——, 2004: Near-surface turbulence in the presence of breaking waves. *J. Phys. Oceanogr.*, **34**, 1067–1086, https://doi.org/10.1175/1520-0485(2004)034<1067:NTITPO>2.0.CO;2.

——, C. J. Zappa, and M. L. Banner, 2008: Spectrally resolved energy dissipation rate and momentum flux of breaking waves. *J. Phys. Oceanogr.*, **38**, 1296–1312, https://doi.org/10.1175/2007JPO3762.1.

Gerbi, G. P., J. H. Trowbridge, E. A. Terray, A. J. Plueddemann, and T. Kukulka, 2009: Observations of turbulence in the ocean surface boundary layer: Energetics and transport. *J. Phys. Oceanogr.*, **39**, 1077–1096, https://doi.org/10.1175/2008JPO4044.1.

Geyer, W. R., 1997: Influence of wind on dynamics and flushing of shallow estuaries. *Estuarine Coastal Shelf Sci.*, **44**, 713–722, https://doi.org/10.1006/ecss.1996.0140.

Greenan, B. J. W., N. S. Oakey, and F. W. Dobson, 2001: Estimates of dissipation in the ocean mixed layer using a quasihorizontal microstructure profiler. *J. Phys. Oceanogr.*, **31**, 992–1004, https://doi.org/10.1175/1520-0485(2001)031<0992:EODITO>2.0.CO;2.

Harcourt, R. R., 2015: An improved second-moment closure model of Langmuir turbulence. *J. Phys. Oceanogr.*, **45**, 84–103, https://doi.org/10.1175/JPO-D-14-0046.1.

Hinze, J. O., 1975: *Turbulence*. 2nd ed. McGraw-Hill, 790 pp.

Hwang, P. A., D. W. Wang, E. J. Walsh, W. B. Krabill, and R. W. Swift, 2000: Airborne measurements of the wavenumber spectra of ocean surface waves. Part II: Directional distribution. *J. Phys. Oceanogr.*, **30**, 2768–2787, https://doi.org/10.1175/1520-0485(2001)031<2768:AMOTWS>2.0.CO;2.

——, J. V. Toporkov, M. A. Sletten, and S. P. Menk, 2013: Mapping surface currents and waves with interferometric synthetic aperture radar in coastal waters: Observations of wave breaking in swell-dominated conditions. *J. Phys. Oceanogr.*, **43**, 563–582, https://doi.org/10.1175/JPO-D-12-0128.1.

Itsweire, E. C., J. R. Koseff, D. A. Briggs, and J. H. Ferziger, 1993: Turbulence in stratified shear flows: Implications for interpreting shear-induced mixing in the ocean. *J. Phys. Oceanogr.*, **23**, 1508–1522, https://doi.org/10.1175/1520-0485(1993)023<1508:TISSFI>2.0.CO;2.

Ivey, G. N., and J. Imberger, 1991: On the nature of turbulence in a stratified fluid. Part I: The energetics of mixing.

J. Phys. Oceanogr., **21**, 650–658, https://doi.org/10.1175/1520-0485(1991)021<0650:OTNOTI>2.0.CO;2.

Johnson, D., 2002: DIWASP, a directional wave spectra toolbox for MATLAB: User manual. Centre for Water Research Rep. WP-1601-DJ (version 1.1), 19 pp.

Jones, N. L., and S. Monismith, 2008a: The influence of whitecapping waves on the vertical structure of turbulence in a shallow estuarine embayment. *J. Phys. Oceanogr.*, **38**, 1563–1580, https://doi.org/10.1175/2007JPO3766.1.

——, and ——, 2008b: Modeling the influence of wave-enhanced turbulence in a shallow tide- and wind-driven water column. *J. Geophys. Res.*, **113**, C03009, https://doi.org/10.1029/2007JC004246.

Kaimal, J. C., J. C. Wyngaard, Y. Izumi, and O. R. Cote, 1972: Spectral characteristics of surface-layer turbulence. *Quart. J. Roy. Meteor. Soc.*, **98**, 563–589, https://doi.org/10.1002/qj.49709841707.

Kantha, L. H., and C. A. Clayson, 1994: An improved mixed layer model for geophysical applications. *J. Geophys. Res.*, **99**, 25 235–25 266, https://doi.org/10.1029/94JC02257.

——, and ——, 2004: On the effect of surface gravity waves on mixing in the oceanic mixed layer. *Ocean Modell.*, **6**, 101–124, https://doi.org/10.1016/S1463-5003(02)00062-8.

Kenyon, K. E., 1969: Stokes drift for random gravity waves. *J. Geophys. Res.*, **74**, 6991–6994, https://doi.org/10.1029/JC074i028p06991.

Kitaigorodskii, S. A., M. A. Donelan, J. L. Lumley, and E. A. Terray, 1983: Wave-turbulence interactions in the upper ocean. Part II: Statistical characteristics of wave and turbulent components of the random velocity field in the marine surface layer. *J. Phys. Oceanogr.*, **13**, 1988–1999, https://doi.org/10.1175/1520-0485(1983)013<1988:WTIITU>2.0.CO;2.

Kleiss, J. M., and W. K. Melville, 2010: Observations of wave breaking kinematics in fetch-limited seas. *J. Phys. Oceanogr.*, **40**, 2575–2604, https://doi.org/10.1175/2010JPO4383.1.

Kundu, P. K., 1980: A numerical investigation of mixed-layer dynamics. *J. Phys. Oceanogr.*, **10**, 220–236, https://doi.org/10.1175/1520-0485(1980)010<0220:ANIOML>2.0.CO;2.

Leibovich, S., 1983: The form and dynamics of Langmuir circulations. *Annu. Rev. Fluid Mech.*, **15**, 391–427, https://doi.org/10.1146/annurev.fl.15.010183.002135.

Li, S., M. Li, G. Gerbi, and J.-B. Song, 2013: Roles of breaking waves and Langmuir circulation in the surface boundary layer of a coastal ocean. *J. Geophys. Res. Oceans*, **118**, 5173–5187, https://doi.org/10.1002/jgrc.20387.

Li, Y., and M. Li, 2011: Effects of winds on stratification and circulation in a partially mixed estuary. *J. Geophys. Res.*, **116**, C12012, https://doi.org/10.1029/2010JC006893.

——, and ——, 2012: Wind-driven lateral circulation in a stratified estuary and its effects on the along-channel flow. *J. Geophys. Res.*, **117**, C09005, https://doi.org/10.1029/2011JC007829.

Luketina, D. A., and J. Imberger, 1989: Turbulence and entrainment in a buoyant surface plume. *J. Geophys. Res.*, **94**, 12 619–12 636, https://doi.org/10.1029/JC094iC09p12619.

Lumley, J. L., and E. A. Terray, 1983: Kinematics of turbulence convected by a random wave field. *J. Phys. Oceanogr.*, **13**, 2000–2007, https://doi.org/10.1175/1520-0485(1983)013<2000:KOTCBA>2.0.CO;2.

Magnaudet, J., and L. Thais, 1995: Orbital rotational motion and turbulence below laboratory wind water waves. *J. Geophys. Res.*, **100**, 757–771, https://doi.org/10.1029/94JC02715.

McWilliams, J. C., P. P. Sullivan, and C.-H. Moeng, 1997: Langmuir turbulence in the ocean. *J. Fluid Mech.*, **334**, 1–30, https://doi.org/10.1017/S0022112096004375.

Mellor, G. L., and T. Yamada, 1982: Development of a turbulence closure model for geophysical fluid problems. *Rev. Geophys.*, **20**, 851–875, https://doi.org/10.1029/RG020i004p00851.

Melsom, A., and Ø. Sætra, 2004: Effects of wave breaking in the near-surface profiles of velocity and turbulent kinetic energy. *J. Phys. Oceanogr.*, **34**, 490–504, https://doi.org/10.1175/2496.1.

Melville, W. K., 1996: The role of surface-wave breaking in air-sea interaction. *Annu. Rev. Fluid Mech.*, **28**, 279–321, https://doi.org/10.1146/annurev.fl.28.010196.001431.

——, F. Veron, and C. White, 2002: The velocity field under breaking waves: Coherent structures and turbulence. *J. Fluid Mech.*, **454**, 203–233, https://doi.org/10.1017/S0022112001007078.

Monismith, S. G., and J. Magnaudet, 1998: On wavy mean flows, Langmuir cells, strain, and turbulence. *Physical Processes in Lakes and Oceans*, J. Imberger, Ed., Coastal and Estuarine Studies Series, Vol. 54, Amer. Geophys. Union, 101–110.

Osborn, T., D. M. Farmer, S. Vagle, S. A. Thorpe, and M. Cure, 1992: Measurements of bubble plumes and turbulence from a submarine. *Atmos.–Ocean*, **30**, 419–440, https://doi.org/10.1080/07055900.1992.9649447.

Phillips, O. M., 1985: Spectral and statistical properties of the equilibrium range in wind-generated gravity waves. *J. Fluid Mech.*, **156**, 505–531, https://doi.org/10.1017/S0022112085002221.

Plant, W. J., 1982: A relationship between wind stress and wave slope. *J. Geophys. Res.*, **87**, 1961–1967, https://doi.org/10.1029/JC087iC03p01961.

Rapp, R. J., and W. K. Melville, 1990: Laboratory measurements of deep-water breaking waves. *Philos. Trans. Roy. Soc. London*, **A331**, 735–800, https://doi.org/10.1098/rsta.1990.0098.

Rieder, K. F., J. A. Smith, and R. A. Weller, 1994: Observed directional characteristics of the wind, wind stress, and surface waves on the open ocean. *J. Geophys. Res.*, **99**, 22 589–22 596, https://doi.org/10.1029/94JC02215.

Rodi, W., 1980: *Turbulence Models and Their Application in Hydraulics.* International Association for Hydraulics Research, 115 pp.

——, 1987: Examples of calculation methods for flow and mixing in stratified fluids. *J. Geophys. Res.*, **92**, 5305–5328, https://doi.org/10.1029/JC092iC05p05305.

Schwendeman, M., J. Thomson, and J. Gemmrich, 2014: Wave breaking dissipation in a young wind sea. *J. Phys. Oceanogr.*, **44**, 104–127, https://doi.org/10.1175/JPO-D-12-0237.1.

Scully, M. E., 2010a: Wind modulation of dissolved oxygen in Chesapeake Bay. *Estuaries Coasts*, **33**, 1164–1175, https://doi.org/10.1007/s12237-010-9319-9.

——, 2010b: The importance of climate variability to wind-driven modulation of hypoxia in Chesapeake Bay. *J. Phys. Oceanogr.*, **40**, 1435–1440, https://doi.org/10.1175/2010JPO4321.1.

——, 2013: Physical controls on hypoxia in Chesapeake Bay: A numerical modeling study. *J. Geophys. Res. Oceans*, **118**, 1239–1256, https://doi.org/10.1002/jgrc.20138.

——, C. Friedrichs, and J. Brubaker, 2005: Control of estuarine stratification and mixing by wind-induced straining of the estuarine density field. *Estuaries*, **28**, 321–326, https://doi.org/10.1007/BF02693915.

——, W. R. Geyer, and J. H. Trowbridge, 2011: The influence of stratification and nonlocal turbulent production on estuarine turbulence: An assessment of turbulence closure with field observations. *J. Phys. Oceanogr.*, **41**, 166–185, https://doi.org/10.1175/2010JPO4470.1.

——, A. W. Fisher, S. E. Suttles, L. P. Sanford, and W. C. Boicourt, 2015: Characterization and modulation of Langmuir circulation in Chesapeake Bay. *J. Phys. Oceanogr.*, **45**, 2621–2639, https://doi.org/10.1175/JPO-D-14-0239.1.

——, J. H. Trowbridge, and A. W. Fisher, 2016: Observations of the transfer of energy and momentum to the oceanic surface layer beneath breaking waves. *J. Phys. Oceanogr.*, **46**, 1823–1837, https://doi.org/10.1175/JPO-D-15-0165.1.

Skyllingstad, E. D., and D. W. Denbo, 1995: An ocean large-eddy simulation of Langmuir circulations and convection in the surface mixed layer. *J. Geophys. Res.*, **100**, 8501–8522, https://doi.org/10.1029/94JC03202.

Soloviev, A., and R. Lukas, 2003: Observation of wave-enhanced turbulence in the near-surface layer of the ocean during TOGA COARE. *Deep-Sea Res. I*, **50**, 371–395, https://doi.org/10.1016/S0967-0637(03)00004-9.

Stacey, M. T., S. G. Monismith, and J. R. Burau, 1999: Observations of turbulence in a partially stratified estuary. *J. Phys. Oceanogr.*, **29**, 1950–1970, https://doi.org/10.1175/1520-0485(1999)029<1950:OOTIAP>2.0.CO;2.

Stips, A., H. Burchard, K. Bolding, H. Prandke, A. Simon, and A. Wuest, 2005: Measurement and simulation of viscous dissipation in the wave affected surface layer. *Deep-Sea Res. II*, **52**, 1133–1155, https://doi.org/10.1016/j.dsr2.2005.01.012.

Sullivan, P. P., J. C. McWilliams, and W. K. Melville, 2004: The oceanic boundary layer driven by wave breaking with stochastic variability. Part 1. Direct numerical simulations. *J. Fluid Mech.*, **507**, 143–174, https://doi.org/10.1017/S0022112004008882.

——, ——, and ——, 2007: Surface gravity wave effects in the oceanic boundary layer: Large-eddy simulation with vortex force and stochastic breakers. *J. Fluid Mech.*, **593**, 405–452, https://doi.org/10.1017/S002211200700897X.

Sutherland, P., and W. K. Melville, 2015: Field measurements of surface and near-surface turbulence in the presence of breaking waves. *J. Phys. Oceanogr.*, **45**, 943–965, https://doi.org/10.1175/JPO-D-14-0133.1.

Tennekes, H., and J. L. Lumley, 1972: *A First Course in Turbulence.* Massachusetts Institute of Technology, 300 pp.

Terray, E. A., M. A. Donelan, Y. C. Agrawal, W. M. Drennan, K. K. Kahma, A. J. Williams, P. A. Hwang, and S. A. Kitaigorodskii, 1996: Estimates of kinetic energy dissipation under breaking waves. *J. Phys. Oceanogr.*, **26**, 792–807, https://doi.org/10.1175/1520-0485(1996)026<0792:EOKEDU>2.0.CO;2.

——, W. M. Drennan, and M. A. Donelan, 1999: The vertical structure of shear and dissipation in the ocean surface layer. *Symp. on the Wind-Driven Air-Sea Interface: Electromagnetic and Acoustic Sensing, Wave-Dynamics and Turbulent Fluxes*, Sydney, Australia, University of New South Wales, 239–245.

Thomson, J., 2012: Wave breaking dissipation observed with SWIFT drifters. *J. Atmos. Oceanic Technol.*, **29**, 1866–1882, https://doi.org/10.1175/JTECH-D-12-00018.1.

——, M. S. Schwendeman, S. F. Zippel, S. Moghimi, J. Gemmrich, and W. E. Rogers, 2016: Wave-breaking turbulence in the ocean surface layer. *J. Phys. Oceanogr.*, **46**, 1857–1870, https://doi.org/10.1175/JPO-D-15-0130.1.

Umlauf, L., and H. Burchard, 2003: A generic length-scale equation for geophysical turbulence models. *J. Mar. Res.*, **61**, 235–265, https://doi.org/10.1357/002224003322005087.

——, and ——, 2005: Second-order turbulence closure models for geophysical boundary layers: A review of recent work. *Cont. Shelf Res.*, **25**, 795–827, https://doi.org/10.1016/j.csr.2004.08.004.

Warner, J. C., W. R. Geyer, and J. A. Lerczak, 2005: Numerical modeling of an estuary: A comprehensive skill assessment. *J. Geophys. Res.*, **110**, C05001, https://doi.org/10.1029/2004JC002691.

Wilcox, D. C., 1988: Reassessment of the scale-determining equation for advanced turbulence models. *AIAA J.*, **26**, 1299–1310, https://doi.org/10.2514/3.10041.

Wilczak, J., S. Oncley, and S. Stage, 2001: Sonic anemometer tilt correction algorithms. *Bound.-Layer Meteor.*, **99**, 127–150, https://doi.org/10.1023/A:1018966204465.

Young, I. R., M. L. Banner, M. A. Donelan, A. V. Babanin, W. K. Melville, F. Veron, and C. McCormick, 2005: An integrated system for the study of wind-wave source terms in finite-depth water. *J. Atmos. Oceanic Technol.*, **22**, 814–831, https://doi.org/10.1175/JTECH1726.1.

Zippel, S., and J. Thomson, 2015: Wave breaking and turbulence at a tidal inlet. *J. Geophys. Res. Oceans*, **120**, 1016–1031, https://doi.org/10.1002/2014JC010025.